ACS APPLIED MATERIALS & INTERFACES

www.acsami.org Research Article

Block Copolymer Derived Vertically Coupled Plasmonic Arrays for Surface-Enhanced Raman Spectroscopy

Goekalp Engin Akinoglu,* Sajjad Husain Mir, Riley Gatensby, Gaulthier Rydzek, and Parvaneh Mokarian-Tabari*

Cite This: https://dx.doi.org/10.1021/acsami.0c03300 Read Online

ACCESS | Metrics & More | Article Recommendations | Supporting Information

ABSTRACT: A surface-enhanced Raman spectroscopy sensing template consisting of gold-covered nanopillars is developed. The plasmonic slab consists of a perforated gold film at the base of the nanopillars and a Babinet complementary dot array on top of the pillars. The nanopillars were fabricated by the incorporation of an iron salt precursor into a self-assembled block copolymer thin film and subsequent reactive ion etching. The preparation is easy, scalable, and cost-effective. We report on the increase in surface-enhanced Raman scattering efficiency for smaller pillar heights and stronger coupling between the dot array and perforated gold film with average enhancement factors as high as 10^7. In addition, the block copolymer-derived templates show an excellent relative standard deviation of 8% in the measurement of the Raman intensity. Finite difference time domain simulations were performed to investigate the nature of the electromagnetic near-field enhancement and to identify plasmonic hot spots.

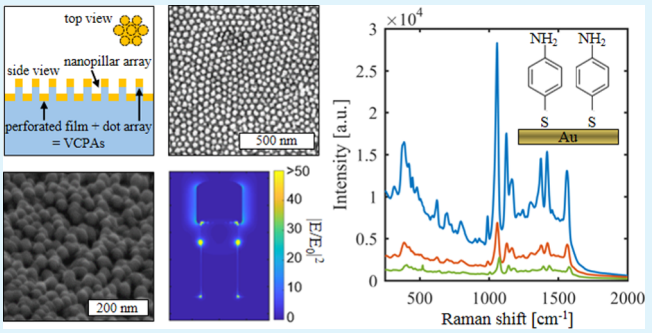

KEYWORDS: *surface-enhanced Raman spectroscopy, block copolymer lithography, nanofabrication, plasmonic nanomaterials, finite difference time domain simulation, 4-aminothiophenol, SERS uniformity*

INTRODUCTION

Surface-enhanced Raman spectroscopy (SERS) is a versatile tool for the detection of analytes in ultralow concentrations. It gives valuable information about molecular vibrations in the vicinity of plasmon active surfaces.[1] It is widely accepted that the main mechanism of the Raman scattering enhancement is the large local electric field amplification at sharp edges or at nanometer-sized gaps between plasmonic particles, so-called plasmonic hot spots.[1] In the last decade, much effort has been concentrated on the fabrication of economically viable SERS sensors with a high density of effective hot spots.[1] These fabrication approaches can be divided into bottom-up and top-down methodologies. Bottom-up approaches use wet chemistry to prepare metallic colloids such as nanospheres,[2] nanorods,[3] or nanostars.[4] Their preparation is easy, scalable, and cost-effective while also providing a strong SERS enhancement. However, a lack of precise control over the nanoparticles shape, size, and arrangement results in varying and non-uniform Raman intensities over the substrate, and reproducibility remains a challenge.[1] Top-down approaches generally rely on lithographic fabrication methods with higher control over the SERS substrate geometrical parameters. However, these generally are of higher cost and have lower throughput. Lithography-based SERS substrates typically consist of metallic dot arrays and their complementary perforated thin films.[5] In recent years, much attention has focused on the study of nanopillar arrays, with their top and base coated by metals, enabling large SERS enhancement factors and increased surface area.[6] This approach allows for recycling of the plasmon-active layer deposited on the nanopillars once contaminated.[7] The perforated metal film at the base of the array can also be used as an electrode for spectrochemistry and electrochemistry.[8] Many methods have been presented for the fabrication of nanopillar arrays for SERS application, including maskless reactive ion etching,[9−11] nanosphere lithography,[12,13] laser interference lithography,[14] E-beam lithography,[15−17] nanoimprint lithography,[18,19] and block copolymer lithography.[7,20]

A common strategy is based on pillar arrays with large aspect ratios on the order of 10:1. After a target analyte is drop-coated on to the SERS substrate and the subsequent solvent evaporates, the pillars aggregate due to surface tension. The result is a strong lateral coupling of the plasmon-active metals deposited on top of the pillars, which deliver a strong SERS enhancement.[7,9−12,20] In addition, hydrophobic pillar arrays

Received: February 20, 2020
Accepted: April 16, 2020

https://dx.doi.org/10.1021/acsami.0c03300
ACS Appl. Mater. Interfaces XXXX, XXX, XXX−XXX

Scheme 1. Fabrication Process for VCPAs[a]

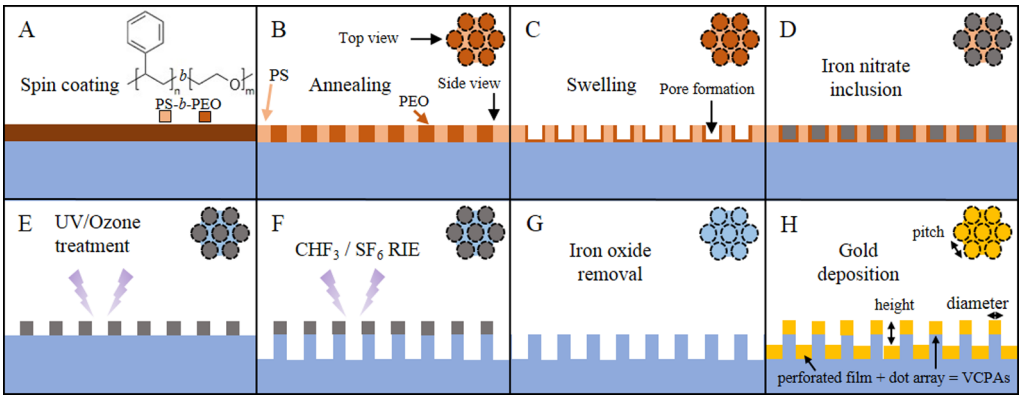

[a](A) Block copolymer is spin cast on silicon, (B) microphase separation of the block copolymer by solvent vapor annealing, and (C) ethanol swelling of the phase-separated film. (D) Incorporation of iron salt into the block copolymer film, (E) polymer removal, and the formation of iron oxide nanodots by a UV/ozone treatment. (F) Iron oxide nanodots are used as an etch mask and pillars are etched into the substrate,(G) iron oxide is removed from the top of the pillars, and (H) gold is deposited on the nanopillar template. The perforated gold film at the base of the pillars and the gold dot array on top of the pillars form vertically coupled plasmonic arrays (VCPAs).

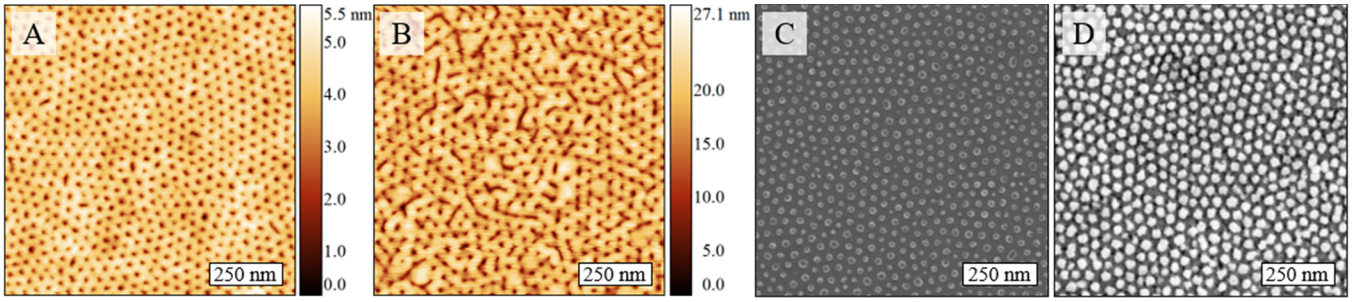

Figure 1. Fabrication process steps: AFM topography images after (A) phase separation of PS-*b*-PEO and (B) swelling of the block copolymer film. Top-down SEM images of (C) iron oxide etch mask, after polymer removal and (D) of VCPAs.

can confine the spread of droplets and consequently increase the analyte concentration locally on the SERS substrate.[21] However, the aggregation-based strategy leads to non-uniform local Raman intensities that can vary by up to a factor of two across the substrate.[7] It is also disadvantageous for *in situ* studies in an aqueous environment and for analytes that require a controlled functionalization of the metal surface.[22]

As an alternative approach, pillar arrays with small height-to-diameter aspect ratios may be used.[15−18,23] These nanopillars enable two types of couplings depending on their geometrical parameters: (i) lateral coupling in between the top of the pillars[23] or (ii) vertical coupling of the metal layers deposited on top of the nanopillars and dewetted gold clusters on the side wall of the nanopillars that typically arise from an inhomogeneous metal deposition process.[15−18] Here, we present SERS substrates fabricated by block copolymer lithography and based on strong vertically coupled plasmonic arrays (VCPAs) between the gold layer on top of the nanopillars and a perforated gold thin film at their base. It is demonstrated that the Raman intensity drastically increases for decreasing gap sizes between the perforated gold thin film and the gold dot array. Previously, nanopillar SERS substrates fabricated by block copolymers have relied on a costly atomic layer deposition intermediate step.[7,20] We show that such arrays can be fabricated by a novel cost-effective and scalable process based on the selective incorporation of iron precursors in microphase-separated block copolymer films to form an etch mask[24] (see Scheme 1).

RESULTS AND DISCUSSION

Sample Fabrication. The optical properties and the SERS enhancement of the VCPAs are governed by the geometrical parameters of the plasmonic slab.[18,25] The best enhancement is achieved when the plasmon resonance is tuned to the laser excitation wavelength. Tuning can be made by adjusting the pillar height through the etch process parameters. The pitch and pillar diameter are defined by the initial etch mask predefined by the block copolymer system. The relative size and structure of the block copolymer film can be varied through altering the molecular weight, volume fraction, and chemical structure of the components of the block copolymer. Here, the polystyrene-*b*-poly(ethylene oxide) (PS-*b*-PEO) block copolymer was used with respective average molecular masses of blocks M_{PS} = 42 kg mol^{-1} and M_{PEO} = 11.5 kg mol^{-1}.[26,27] This block copolymer system has been previously well studied, and the derived pattern shows large scale uniformity, which has been confirmed by grazing incidence small-angle X-ray scattering.[28−32] A 1 wt % block copolymer solution in toluene was spun cast onto a silicon substrate for 30 s at 3000 rpm, which was followed by solvent vapor annealing in a glass jar in a toluene atmosphere for 80 min at 50 °C. Thermal solvent vapor annealing facilitates the mobility of the polymer chains so that the cast film can restructure into a more stable state in thermal equilibrium. As a result, the block copolymer phase separates into hexagonal-ordered PEO domains in a PS matrix, observed by AFM analysis (Figure 1A and a corresponding AFM profile line in

https://dx.doi.org/10.1021/acsami.0c03300
ACS Appl. Mater. Interfaces XXXX, XXX, XXX−XXX

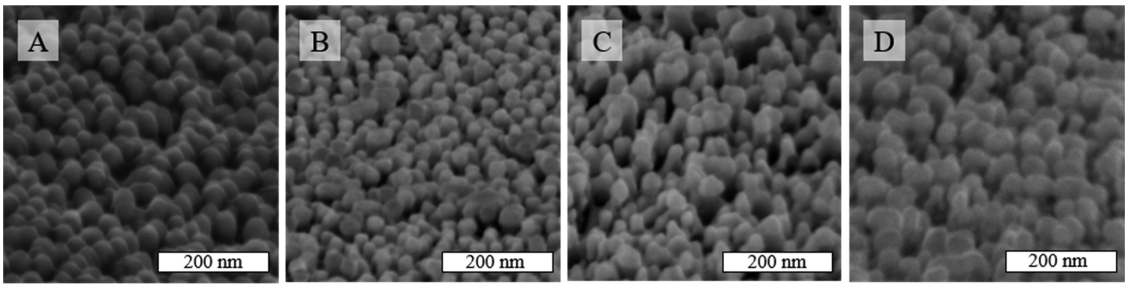

Figure 2. SEM images of VCPAS of varying heights imaged at a 70° angle. Pillar heights are (A) 55 nm, (B) 65 nm, (C) 74 nm, and (D) 91 nm.

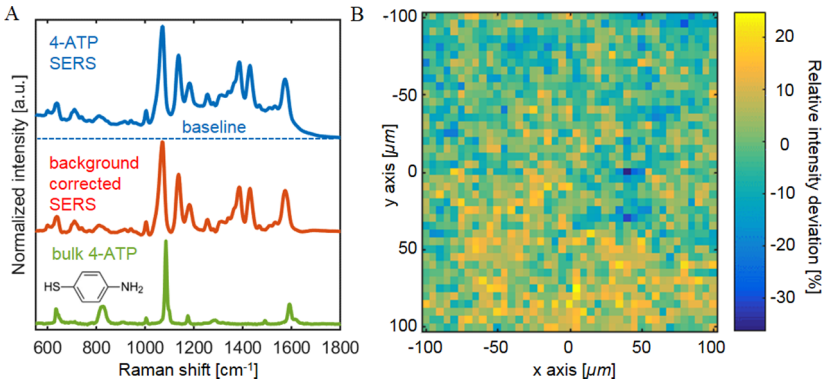

Figure 3. (A) SERS, background-corrected SERS, and Raman spectra of 4-ATP. The spectra were normalized to their maximum Raman scattering intensity for better visual comparison. (B) 200 μm × 200 μm map of the background-corrected Raman intensity deviation to its mean value. C−S, 7(a$(a_1)_3$ stretch vibration peak at 1075 cm^{-1} and a 5× objective (NA = 0.25) with a 4 μm laser diameter were used with a 5 μm mapping resolution.

Figure S1). Next, phase-separated film is swelled in anhydrous ethanol for 14 h at 40 °C to expand the depth of the PEO domains from up to 5.5nm to up to 27.1 nm (Figure 1B and a corresponding AFM profile line in Figure S2).

The increased dimensions of the pores enables the incorporation of larger volumes of the final etch mask material into the polymer domains. Adding this material is essential because the etch selectivity of the polymer is low compared to the substrate.[24] Therefore, a freshly prepared 0.4 wt % iron (III) nitrate solution in anhydrous ethanol was spun cast (30 s, 3000 rpm) on the substrate to fill the PEO pores. Organic materials were removed by a 3 h UV/ozone exposure, which also oxidizes the iron inside the cavities.[29] The fabricated iron oxide arrays have an average dot diameter of d = 28.4 nm ± 4.4 nm and a pitch of a = 42.3 nm ± 3 nm (Figure 1C, histograms for the diameter and pitch in Figures S3 and S4, and an AFM analysis in Figure S5). A small pitch compared to the diameter is favorable because it increases the pillar density and therefore hot spot formation for SERS. It also results in lateral coupling between the apexes of the pillars. The nanopillars are created by reactive ion etching in a fluorinated plasma, where the pillar height is well controlled by adjusting the etch duration (see Figure S6 for SEM top-down views with different magnifications). To prevent cross contamination of the SERS spectra due to carbon fluoride, the silicon etching is followed by an oxygenated plasma cleaning step. Finally, any remaining iron oxide dots are removed through a nitric acid wet etch. The VCPAs are formed by depositing a 5 nm titanium adhesion layer and a 35 nm plasmon active gold layer onto the nanopillar template. Gold has inferior SERS enhancement factors compared to silver but is stable under ambient conditions and does not suffers from oxidation.[33]

The plasmonic slab consists of a perforated gold film at the base of the pillars and a dot array on top of the pillars. The gold dots on top of the nanopillars extend slightly over the silicon nanopillar base and have an average diameter of d = 33.7 nm ± 7.1 nm (Figure 1D and a histogram for the diameter in Figure S7). This is advantageous since it increases the surface area at the main hot spot locations. Furthermore, the small standard deviation of the gold dot diameter reduces inhomogeneous broadening of the plasmon resonance that can lower the SERS intensity.[34] A series of angled views of the VCPAs with different heights is shown in Figure 2.

SERS Measurements. 4-aminothiophenol (4-ATP) was selected as a probe molecule, as the thiol group can form covalent bonds with the gold surface. Moreover, the molecule is already used as a SERS probe and the vibrational bands at the finger print region have been assigned.[35] A special feature of the 4-ATP molecule is its capability to oxidize to 4,4′-dimercaptoazobenzene during a SERS experiment.[36] The VCPAs were immersed into 1 mM 4-ATP for 12 h to self-assemble a single monolayer onto the gold surface and were then thoroughly rinsed with milli-Q water to remove any excess molecules. In this study, we focused only on the C−S bond stretching vibration coupled to the 7a$(a_1)_3$ benzene ring stretching vibration mode at the ∼1075 cm^{-1} peak, as it has similar SERS line shapes and intensities for both molecules.[36] In Figure 3A, the normalized SERS spectra and conventional Raman signal of bulk 4-ATP is shown. The strongest peak is from the C−S, 7a$(a_1)_3$ stretch vibration at ∼1075 cm^{-1}. The SERS spectra show a typical broad continuum background, and the line shapes of the molecules are broadened compared to the bulk 4-ATP Raman spectrum,[37] which is especially useful when using low resolution Raman spectroscopy. To

https://dx.doi.org/10.1021/acsami.0c03300
ACS Appl. Mater. Interfaces XXXX, XXX, XXX−XXX

demonstrate that our block copolymer-derived templates are a reliable platform for SERS, a 200 μm × 200 μm map of the background-corrected SERS intensity was measured. It showed an average relative standard deviation of 8% (Figure 3B). Further, the effect of the nanopillar height on the SERS enhancement factor was investigated (Figure 4). It is assumed

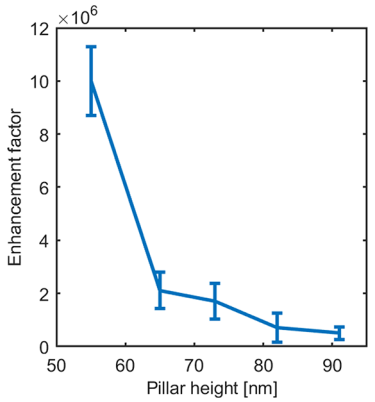

Figure 4. Experimental enhancement factor of VCPAs with different pillar heights. The metal thickness coated on the nanopillar array template is 40 nm.

that the gold surface of the VCPAs is fully covered by 4-ATP molecules, and all the molecules contribute to the Raman signal. The SERS enhancement drastically increases for shorter pillar heights and smaller interslab gaps. Generally, the electric near-field enhancement increases exponentially with a decreasing plasmonic gap size.[38] However, it will also shift the plasmon resonance position, and a careful optimization must be done to adjust the plasmon resonance to the laser wavelength.[38] Hence, smaller plasmonic gaps will generally enhance the Raman intensity, and therefore, smaller pillar heights should perform better.[38,39] The strongest experimental enhancement factor is calculated to be 1×10^7 for nanopillars with h = 55 nm and a gap between the metal films below 15 nm. We note that the size of the plasmonic gaps is large enough to enable the functionalization of the gold surface and leave enough space to be accessible for larger macromolecules such as proteins.[40] Furthermore, the calculated enhancement factors are the average, assuming that all the molecules contribute equally to the SERS intensity. If one applies an assumption (as made in ref 19) that only a small fraction of the total molecules that are in the plasmonic hot spots contribute to the Raman signal, then the SERS enhancement factor can be several magnitudes higher.[9] To put this into perspective, Le Ru *et al.*[41] demonstrated that enhancement factors as low as 10^7 are sufficient for single molecule SERS signals, whereas typical maximum single molecule SERS experiments are performed with enhancement factors at the order of ~10^{10}. Hence, we anticipate that our VCPAs should be capable of single molecule spectroscopy.[41]

FDTD Simulation. To investigate the origin of the large enhancement factor, finite difference time domain (FDTD) simulations were performed to predict the nature of the plasmonic hot spots. In the simplest approximation, the SERS enhancement scales with the fourth power of the electric field enhancement $I_{SERS} \propto < E^4/E_0^4 >$, where E is the electric field at the surface of the plasmonic structure, which is normalized to the electric field of the incident light E_0. At first, simple nanopillars without gold were simulated. Figure 5A shows the cross section of the electric field enhancement. As expected, the near-field enhancement is negligible without plasmon resonance. Further simulations added (cumulatively) gold dots on top of the nanopillars (see cross section in Figure 5B), a perforated gold thin film at the base of the nanopillars (Figure 5C), and VCPAs (Figure 5D) at plasmon resonance. Clearly, there is a strong near-field enhancement in between the vertical gap of the plasmonic slabs. In Figure 5E, the near-field enhancement as a function of wavelength is shown. The VCPAs feature larger electric field enhancements than the respective individual perforated film and dot array, and the plasmon resonance and near-field enhancement is also broader.

The strong enhancement of the VCPAs is attributed to Babinet's principle.[42] Babinet's principle states that the transmittance (T) of a slab and its complementary counterpart (T_C) should fulfill $T + T_C = 1$. This indicates that the resonance position of the perforated film and that of the dot

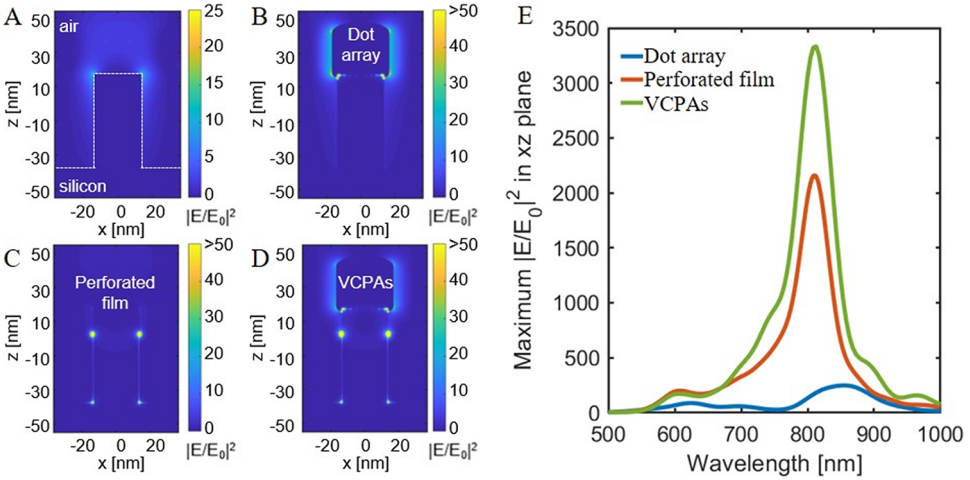

Figure 5. Cross section of the simulated electric field enhancement (A–D). (A) Silicon nanopillar with 55 nm height. (B) Gold dot array on top of the nanopillars, (C) nanopillars perforating a thin gold film at plasmon resonance, and (D) VCPAs at plasmon resonance. (E) Electric field enhancement as a function of wavelength for dot arrays, perforated gold film, and VCPAs. The VCPAs perform equal or better than the respective perforated film and dot array for any wavelength between 500–1000 nm.

https://dx.doi.org/10.1021/acsami.0c03300
ACS Appl. Mater. Interfaces XXXX, XXX, XXX−XXX

array should be somewhat similar. Therefore, the plasmonic resonance can be seen as analogous to the coupling of nanoparticle dimers.[43] Accordingly, the plasmon coupling can be tuned by the gap size between the perforated film and dot array[42] and therefore also the electric field enhancement.

CONCLUSIONS

In this work, we investigated the Raman enhancement of strong vertically coupled plasmonic arrays for SERS sensors fabricated by block copolymer lithography. These structures demonstrate enhancement factors up to 1×10^7 with a standard deviation of the Raman intensity of 8%. We showed that with decreasing pillar heights and gap sizes of the individual plasmonic slabs, the Raman intensity significantly increases. FDTD simulations predict that the electric field enhancement due to the VCPAs is greater than that of the individual contributions of the perforated gold film and gold dot array.

MATERIALS AND METHODS

Sample Fabrication. PS-*b*-PEO with average molecular masses of blocks M_{PS} = 42 kg mol^{-1} and M_{PEO} = 11.5 kg mol^{-1} was purchased from Polymer Source Inc. A 1 wt % PS-*b*-PEO solution was prepared in toluene, and subsequently spin cast on a silicon substrate for 30 s at 3000 rpm. The phase separation of the block copolymer films was performed by solvent vapor annealing in a glass jar in a toluene atmosphere for 80 min and at 50 °C. The glass transition temperature of the PS blocks (103 °C) is higher than the PEO crystal melting temperature (55 °C). Therefore, the PEO block crystallization is confined within the PS matrix. Subsequently, the self-assembled block copolymer films were swelled in anhydrous ethanol for 14 h at 40 °C and then dried in a nitrogen stream. A 0.4 wt % iron (III) nitrate solution in anhydrous ethanol was spin cast (30s, 3000 rpm) on to the phase-separated block copolymer films. To obtain the iron oxide nanodot etch mask, the polymer organics were removed by UV/ozone exposure for 3 h. Reactive ion etching was performed in an OIPT Plasmalab System100 ICP180 etcher (Oxford Instruments) on the iron oxide dot pattern. The chamber atmosphere consisted of CHF_3, SF_6, and O_2 with a 9:1:1 gas ratio and a chamber pressure of 15 mTor. The ICP power was 1200 W, and the RF RIE bias power was 35 W. The pillar heights were controlled by etch time. Next, the substrates were immersed for 10 min in 10% nitric acid to remove any remaining nanodot mask. Titanium (5 nm) and gold (35 nm) films were deposited using a Temescal FC-2000 electron beam evaporation system with a chamber pressure of 10^{-6} mbar. The samples were at a full meter distance from the metal source, which allowed a nearly perpendicular metal deposition to produce a perforated metal film at the base of the pillars and a dot array on top of the pillars with occasionally small gold clusters hinged at the side wall. As the pitch and the diameter of the particles are determined by the block copolymer system the gold surface area of the VCPAs does not significantly differ for the different pillar heights.

The sizes of the iron oxide hard mask particles and gold dots on top of the nanopillars have been determined by a particle size distribution analysis. The pitch has been determined by neighboring particle distance distribution analysis. For the distribution analysis, more than 2000 particles were considered. Subsequently, the pillar heights were determined from 70° tilted SEM images under consideration of the visual plane at this angle via the formula $\text{height} = \frac{\text{length}_{\text{tilt}}}{\cos(70°)}$ (Figure S8).

Raman Spectroscopy. SERS spectra were collected with a XploRA Raman spectrometer equipped with a 785 nm wavelength laser. The Raman microscope was calibrated with the 520 cm^{-1} silicon peak from a flat silicon surface. The power was set to 0.54 mW. A 100× objective (NA = 0.9) was used with a beam focus width of 1 μm. The integration times were 5 s with five accumulations for each spectrum. Ten spectra from different spots were averaged. The baseline correction was performed with the Matlab 2018a software and the Msbackadj function. The enhancement factor was estimated with following expression

$$EF = \frac{I_{SERS}/N_{SERS}}{I_{REF}/N_{REF}}$$

where I_{SERS} and I_{REF} are the Raman intensities, and N_{SERS} and N_{REF} are the probed molecules for the SERS and reference measurement, respectively. For N_{SERS}, all molecules self-assembled on the gold surface of the VCPAs are counted with a surface packing density of 0.20 nm^2 per molecule.[44] The effective VCPAs surface is estimated to be two times larger than the corresponding flat surface, which leads to an estimate of 7.85×10^6 molecules probes. N_{REF} is calculated by collecting a spectra of bulk 4-ATP with a molecular density of 1.18 g/cm^3. Assuming a laser interaction volume of ∼15 μm^2 and a molecular weight of 125.189 g/mol, we calculated N_{REF} to be 8.8×10^{10}. The mapping data presented in Figure 3B were collected with 785 nm wavelength and 5× objective with a 4 μm laser diameter and 5 μm resolution. Two adjacent 200 μm × 100 μm (the full range of our Piezo stage) regions were measured and subsequently merged for further analysis.

FDTD Simulation. The electric field was simulated with the FDTD method using the open-source software package MEEP.[45] The dielectric function of gold was described by a Lorentz−Drude model using experimental data obtained from Rakić *et al.*[46] A periodic boundary was placed in all dimensions, and an artificial absorber layer was placed parallel to the plasmonic array at the end of the simulation cell to block transmission through the cell. The nanostructures were placed in the middle of the simulation cell (z = 0). The plasmonic arrays and nanopillars were hexagonally arranged (Figure S9). For simplicity, the titanium adhesion layer was omitted from the simulation. The electric near-field cross sections were simulated over a broad spectrum. The maximum value was extracted for each cross section and plotted versus the wavelength.

ASSOCIATED CONTENT

Supporting Information

The Supporting Information is available free of charge at https://pubs.acs.org/doi/10.1021/acsami.0c03300.

AFM profile lines of the phase-separated PS-*b*-PEO film, AFM profile lines of the swelled PS-*b*-PEO film, particle size distribution of the iron oxide dot array, pitch distribution analysis of the iron oxide dot array, AFM analysis of the iron oxide dot array, SEM top-down view of etched nanopillars with different magnifications, particle size distribution of gold dots on top of the nanopillars, 70° tilted SEM pictures of VCPAs at a defect zone and FDTD simulation cell (PDF)

AUTHOR INFORMATION

Corresponding Authors

Goekalp Engin Akinoglu − *Advanced Materials and BioEngineering Research Centre (AMBER) and The School of Chemistry, Trinity College Dublin, The University of Dublin, Dublin 2, Ireland; Freie Universität Berlin, Department of Physics, 14195 Berlin, Germany;* orcid.org/0000-0002-6166-4682; Email: akinoglg@tcd.ie

Parvaneh Mokarian-Tabari − *Advanced Materials and BioEngineering Research Centre (AMBER) and The School of Chemistry, Trinity College Dublin, The University of Dublin, Dublin 2, Ireland*; Email: parvaneh.mokarian@tcd.ie

Authors

Sajjad Husain Mir − *Advanced Materials and BioEngineering Research Centre (AMBER) and The School of Chemistry,*

https://dx.doi.org/10.1021/acsami.0c03300
ACS Appl. Mater. Interfaces XXXX, XXX, XXX−XXX

Trinity College Dublin, The University of Dublin, Dublin 2, Ireland; orcid.org/0000-0001-8416-3891

Riley Gatensby − *Advanced Materials and BioEngineering Research Centre (AMBER) and The School of Chemistry, Trinity College Dublin, The University of Dublin, Dublin 2, Ireland*

Gaulthier Rydzek − *Advanced Materials and BioEngineering Research Centre (AMBER) and The School of Chemistry, Trinity College Dublin, The University of Dublin, Dublin 2, Ireland*

Complete contact information is available at: https://pubs.acs.org/10.1021/acsami.0c03300

Notes

The authors declare no competing financial interest.

■ ACKNOWLEDGMENTS

This project has received funding in part from the European Union's Horizon 2020 Research and Innovation programme under grant agreement no. 760915 (SUN-PILOT),in part by Science Foundation Ireland (SFI) under grant no. 12/RC/2278_P2 and in part by Enterprise Ireland. S.H.M. gratefully received funding from the European Union's Horizon 2020 Research and Innovation programme under the EDGE Marie Skłodowska-Curie grant agreement no. 713567. We gratefully acknowledge the Advanced Microscopy Laboratory (AML), Trinity College Dublin for access to their SEM facilities. All calculations were performed on the Kelvin cluster maintained by the Trinity Centre for High Performance Computing. This cluster was funded through grants from the Higher Education Authority of Ireland, through its PRTLI program. The authors gratefully thank Prof. Reich and Prof. Morris for full access to their labs and equipment. The authors also want to thank Brian Jennings, Neal O'Hara, Sören Waßerroth, Ömer Akay, and Georgy Gordev for fruitful discussion or technical support.

■ REFERENCES

(1) Langer, J.; Jimenez de Aberasturi, D.; Aizpurua, J.; Alvarez-Puebla, R. A.; Auguié, B.; Baumberg, J. J.; Bazan, G. C.; Bell, S. E. J.; Boisen, A.; Brolo, A. G.; Choo, J.; Cialla-May, D.; Deckert, V.; Fabris, L.; Faulds, K.; García de Abajo, F. J.; Goodacre, R.; Graham, D.; Haes, A. J.; Haynes, C. L.; Huck, C.; Itoh, T.; Käll, M.; Kneipp, J.; Kotov, N. A.; Kuang, H.; Le Ru, E. C.; Lee, H. K.; Li, J.-F.; Ling, X. Y.; Maier, S. A.; Mayerhöfer, T.; Moskovits, M.; Murakoshi, K.; Nam, J.-M.; Nie, S.; Ozaki, Y.; Pastoriza-Santos, I.; Perez-Juste, J.; Popp, J.; Pucci, A.; Reich, S.; Ren, B.; Schatz, G. C.; Shegai, T.; Schlücker, S.; Tay, L.-L.; Thomas, K. G.; Tian, Z.-Q.; Van Duyne, R. P.; Vo-Dinh, T.; Wang, Y.; Willets, K. A.; Xu, C.; Xu, H.; Xu, Y.; Yamamoto, Y. S.; Zhao, B.; Liz-Marzán, L. M. Present and Future of Surface Enhanced Raman Scattering. *ACS Nano* **2020**, *14*, 28−117.

(2) Tian, F.; Bonnier, F.; Casey, A.; Shanahan, A. E.; Byrne, H. J. Surface enhanced Raman scattering with gold nanoparticles: effect of particle shape. *Anal. Methods* **2014**, *6*, 9116−9123.

(3) Orendorff, C. J.; Gearheart, L.; Jana, N. R.; Murphy, C. J. Aspect ratio dependence on surface enhanced Raman scattering using silver and gold nanorod substrates. *Phys. Chem. Chem. Phys.* **2006**, *8*, 165−170.

(4) Khoury, C. G.; Vo-Dinh, T. Gold nanostars for surface-enhanced Raman scattering: synthesis, characterization and optimization. *J. Phys. Chem. C* **2008**, *112*, 18849−18859.

(5) Yu, Q.; Guan, P.; Qin, D.; Golden, G.; Wallace, P. M. Inverted Size-Dependence of Surface-Enhanced Raman Scattering on Gold Nanohole and Nanodisk Arrays. *Nano Lett.* **2008**, *8*, 1923−1928.

(6) Oh, Y.-J.; Kang, M.; Park, M.; Jeong, K.-H. Engineering hot spots on plasmonic nanopillar arrays for SERS: A review. *BioChip J.* **2016**, *10*, 297−309.

(7) Wu, K.; Li, T.; Schmidt, M. S.; Rindzevicius, T.; Boisen, A.; Ndoni, S. Gold Nanoparticles Sliding on Recyclable Nanohoodoos—Engineered for Surface-Enhanced Raman Spectroscopy. *Adv. Funct. Mater.* **2018**, *28*, 1704818.

(8) Sanger, K.; Durucan, O.; Wu, K.; Thilsted, A. H.; Heiskanen, A.; Rindzevicius, T.; Schmidt, M. S.; Zór, K.; Boisen, A. Large-Scale, Lithography-Free Production of Transparent Nanostructured Surface for Dual-Functional Electrochemical and SERS Sensing. *ACS Sens.* **2017**, *2*, 1869−1875.

(9) Schmidt, M. S.; Hübner, J.; Boisen, A. Large area fabrication of leaning silicon nanopillars for surface enhanced Raman spectroscopy. *Adv. Mater.* **2012**, *24*, OP11−OP18.

(10) Wu, K.; Rindzevicius, T.; Schmidt, M. S.; Mogensen, K. B.; Xiao, S.; Boisen, A. Plasmon resonances of Ag capped Si nanopillars fabricated using mask-less lithography. *Opt. Express* **2015**, *23*, 12965−12978.

(11) Yang, J.; Palla, M.; Bosco, F. G.; Rindzevicius, T.; Alstrøm, T. S.; Schmidt, M. S.; Boisen, A.; Ju, J.; Lin, Q. Surface-Enhanced Raman Spectroscopy Based Quantitative Bioassay on Aptamer-Functionalized Nanopillars Using Large-Area Raman Mapping. *ACS Nano* **2013**, *7*, 5350−5359.

(12) Kara, S. A.; Keffous, A.; Giovannozzi, A. M.; Rossi, A. M.; Cara, E.; D'Ortenzi, L.; Sparnacci, K.; Boarino, L.; Gabouze, N.; Soukane, S. Fabrication of flexible silicon nanowires by self-assembled metal assisted chemical etching for surface enhanced Raman spectroscopy. *RSC Adv.* **2016**, *6*, 93649−93659.

(13) Men, D.; Wu, Y.; Wang, C.; Xiang, J.; Yang, G.; Wan, C.; Zhang, H. Wafer-Scale Hierarchical Nanopillar Arrays Based on Au Masks and Reactive Ion Etching for Effective 3D SERS Substrate. *Materials* **2018**, *11*, 239.

(14) Gartia, M. R.; Xu, Z.; Behymer, E.; Nguyen, H.; Britten, J. A.; Larson, C.; Miles, R.; Bora, M.; Chang, A. S.; Bond, T. C.; Liu, G. L. Rigorous surface enhanced Raman spectral characterization of large-area high-uniformity silver-coated tapered silica nanopillar arrays. *Nanotechnology* **2010**, *21*, 395701.

(15) Caldwell, J. D.; Glembocki, O.; Bezares, F. J.; Bassim, N. D.; Rendell, R. W.; Feygelson, M.; Ukaegbu, M.; Kasica, R.; Shirey, L.; Hosten, C. Plasmonic nanopillar arrays for large-area, high-enhancement surface-enhanced Raman scattering sensors. *ACS Nano* **2011**, *5*, 4046−4055.

(16) Caldwell, J. D.; Glembocki, O. J.; Bezares, F. J.; Kariniemi, M. I.; Niinistö, J. T.; Hatanpää, T. T.; Rendell, R. W.; Ukaegbu, M.; Ritala, M. K.; Prokes, S. M.; Hosten, C. M.; Leskelä, M. A.; Kasica, R. Large-area plasmonic hot-spot arrays: sub-2 nm interparticle separations with plasma-enhanced atomic layer deposition of Ag on periodic arrays of Si nanopillars. *Opt. Express* **2011**, *19*, 26056−26064.

(17) Bezares, F. J.; Caldwell, J. D.; Glembocki, O.; Rendell, R. W.; Feygelson, M.; Ukaegbu, M.; Kasica, R.; Shirey, L.; Bassim, N. D.; Hosten, C. The Role of Propagating and Localized Surface Plasmons for SERS Enhancement in Periodic Nanostructures. *Plasmonics* **2012**, *7*, 143−150.

(18) Li, W.-D.; Ding, F.; Hu, J.; Chou, S. Y. Three-dimensional cavity nanoantenna coupled plasmonic nanodots for ultrahigh and uniform surface-enhanced Raman scattering over large area. *Opt. Express* **2011**, *19*, 3925−3936.

(19) Hu, M.; Ou, F. S.; Wu, W.; Naumov, I.; Li, X.; Bratkovsky, A. M.; Williams, R. S.; Li, Z. Gold nanofingers for molecule trapping and detection. *J. Am. Chem. Soc.* **2010**, *132*, 12820−12822.

(20) Li, T.; Wu, K.; Rindzevicius, T.; Wang, Z.; Schulte, L.; Schmidt, M. S.; Boisen, A.; Ndoni, S. Wafer-Scale Nanopillars Derived from Block Copolymer Lithography for Surface-Enhanced Raman Spectroscopy. *ACS Appl. Mater. Interfaces* **2016**, *8*, 15668−15675.

(21) De Angelis, F.; Gentile, F.; Mecarini, F.; Das, G.; Moretti, M.; Candeloro, P.; Coluccio, M. L.; Cojoc, G.; Accardo, A.; Liberale, C.; Zaccaria, R. P.; Perozziello, G.; Tirinato, L.; Toma, A.; Cuda, G.; Cingolani, R.; Di Fabrizio, E. Breaking the diffusion limit with super-

hydrophobic delivery of molecules to plasmonic nanofocusing SERS structures. *Nat. Photonics* **2011**, *5*, 682.
(22) Kamińska, A.; Witkowska, E.; Winkler, K.; Dzięcielewski, I.; Weyher, J. L.; Waluk, J. Detection of Hepatitis B virus antigen from human blood: SERS immunoassay in a microfluidic system. *Biosens. Bioelectron.* **2015**, *66*, 461−467.
(23) Li, J.; Chen, C.; Jans, H.; Xu, X.; Verellen, N.; Vos, I.; Okumura, Y.; Moshchalkov, V. V.; Lagae, L.; Van Dorpe, P. 300 mm Wafer-level, ultra-dense arrays of Au-capped nanopillars with sub-10 nm gaps as reliable SERS substrates. *Nanoscale* **2014**, *6*, 12391−12396.
(24) Cummins, C.; Ghoshal, T.; Holmes, J. D.; Morris, M. A. Strategies for inorganic incorporation using neat block copolymer thin films for etch mask function and nanotechnological application. *Adv. Mater.* **2016**, *28*, 5586−5618.
(25) Li, W.-D.; Hu, J.; Chou, S. Y. Extraordinary light transmission through opaque thin metal film with subwavelength holes blocked by metal disks. *Opt. Express* **2011**, *19*, 21098−21108.
(26) Ghoshal, T.; Senthamaraikannan, R.; Shaw, M. T.; Holmes, J. D.; Morris, M. A. "In situ" hard mask materials: a new methodology for creation of vertical silicon nanopillar and nanowire arrays. *Nanoscale* **2012**, *4*, 7743−7750.
(27) Mokarian-Tabari, P.; Vallejo-Giraldo, C.; Fernandez-Yague, M.; Cummins, C.; Morris, M. A.; Biggs, M. J. P. Nanoscale neuroelectrode modification via sub-20 nm silicon nanowires through self-assembly of block copolymers. *J. Mater. Sci.: Mater. Med.* **2015**, *26*, 120.
(28) Giraud, E. C.; Mokarian-Tabari, P.; Toolan, D. T. W.; Arnold, T.; Smith, A. J.; Howse, J. R.; Topham, P. D.; Morris, M. A. Highly Ordered Titanium Dioxide Nanostructures via a Simple One-Step Vapor-Inclusion Method in Block Copolymer Films. *ACS Appl. Nano Mater.* **2018**, *1*, 3426−3434.
(29) Ghoshal, T.; O'Connell, J.; Sinturel, C.; Andreazza, P.; Holmes, J. D.; Morris, M. A. Solvent mediated inclusion of metal oxide into block copolymer nanopatterns: Mechanism of oxide formation under UV-Ozone treatment. *Polymer* **2019**, *173*, 197−204.
(30) Darko, C.; Botiz, I.; Reiter, G.; Breiby, D. W.; Andreasen, J. W.; Roth, S. V.; Smilgies, D.-M.; Metwalli, E.; Papadakis, C. M. Crystallization in diblock copolymer thin films at different degrees of supercooling. *Phys. Rev. E* **2009**, *79*, No. 041802.
(31) Metwalli, E.; Perlich, J.; Wang, W.; Diethert, A.; Roth, S. V.; Papadakis, C. M.; Müller-Buschbaum, P. Morphology of Semicrystalline Diblock Copolymer Thin Films upon Directional Solvent Vapor Flow. *Macromol. Chem. Phys.* **2010**, *211*, 2102−2108.
(32) Zhang, M.; Yang, L.; Yurt, S.; Misner, M. J.; Chen, J.-T.; Coughlin, E. B.; Venkataraman, D.; Russell, T. P. Highly Ordered Nanoporous Thin Films from Cleavable Polystyrene-block-poly(ethylene oxide). *Adv. Mater.* **2007**, *19*, 1571−1576.
(33) Fan, M.; Lai, F.-J.; Chou, H.-L.; Lu, W.-T.; Hwang, B.-J.; Brolo, A. G. Surface-enhanced Raman scattering (SERS) from Au:Ag bimetallic nanoparticles: the effect of the molecular probe. *Chem. Sci.* **2013**, *4*, 509−515.
(34) Eustis, S.; El-Sayed, M. A. Determination of the aspect ratio statistical distribution of gold nanorods in solution from a theoretical fit of the observed inhomogeneously broadened longitudinal plasmon resonance absorption spectrum. *J. Appl. Phys.* **2006**, *100*, No. 044324.
(35) Kim, K.; Yoon, J. K. Raman Scattering of 4-Aminobenzenethiol Sandwiched between Ag/Au Nanoparticle and Macroscopically Smooth Au Substrate. *J. Phys. Chem. B* **2005**, *109*, 20731−20736.
(36) Huang, Y.-F.; Zhu, H.-P.; Liu, G.-K.; Wu, D.-Y.; Ren, B.; Tian, Z.-Q. When the signal is not from the original molecule to be detected: chemical transformation of para-aminothiophenol on Ag during the SERS measurement. *J. Am. Chem. Soc.* **2010**, *132*, 9244−9246.
(37) Mahajan, S.; Cole, R. M.; Speed, J. D.; Pelfrey, S. H.; Russell, A. E.; Bartlett, P. N.; Barnett, S. M.; Baumberg, J. J. Understanding the Surface-Enhanced Raman Spectroscopy "Background". *J. Phys. Chem. C* **2010**, *114*, 7242−7250.
(38) Ding, S.-Y.; You, E.-M.; Tian, Z.-Q.; Moskovits, M. Electromagnetic theories of surface-enhanced Raman spectroscopy. *Chem. Soc. Rev.* **2017**, *46*, 4042−4076.
(39) Fu, Q.; Zhan, Z.; Dou, J.; Zheng, X.; Xu, R.; Wu, M.; Lei, Y. Highly Reproducible and Sensitive SERS Substrates with Ag Inter-Nanoparticle Gaps of 5 nm Fabricated by Ultrathin Aluminum Mask Technique. *ACS Appl. Mater. Interfaces* **2015**, *7*, 13322−13328.
(40) Ataka, K.; Heberle, J. Functional vibrational spectroscopy of a cytochrome c monolayer: SEIDAS probes the interaction with different surface-modified electrodes. *J. Am. Chem. Soc.* **2004**, *126*, 9445−9457.
(41) Le Ru, E. C.; Blackie, E.; Meyer, M.; Etchegoin, P. G. Surface enhanced Raman scattering enhancement factors: a comprehensive study. *J. Phys. Chem. C* **2007**, *111*, 13794−13803.
(42) Akinoglu, G. E.; Akinoglu, E. M.; Kempa, K.; Giersig, M. Plasmon resonances in coupled Babinet complementary arrays in the mid-infrared range. *Opt. Express* **2019**, *27*, 22939−22950.
(43) Nordlander, P.; Oubre, C.; Prodan, E.; Li, K.; Stockman, M. I. Plasmon hybridization in nanoparticle dimers. *Nano Lett.* **2004**, *4*, 899−903.
(44) Gole, A.; Sainkar, S. R.; Sastry, M. Electrostatically Controlled Organization of Carboxylic Acid Derivatized Colloidal Silver Particles on Amine-Terminated Self-Assembled Monolayers. *Chem. Mater.* **2000**, *12*, 1234−1239.
(45) Oskooi, A. F.; Roundy, D.; Ibanescu, M.; Bermel, P.; Joannopoulos, J. D.; Johnson, S. G. MEEP: A flexible free-software package for electromagnetic simulations by the FDTD method. *Comput. Phys. Commun.* **2010**, *181*, 687−702.
(46) Rakić, A. D.; Djurišić, A. B.; Elazar, J. M.; Majewski, M. L. Optical properties of metallic films for vertical-cavity optoelectronic devices. *Appl. Opt.* **1998**, *37*, 5271−5283.

https://dx.doi.org/10.1021/acsami.0c03300
ACS Appl. Mater. Interfaces XXXX, XXX, XXX−XXX